Seismological Characterization of the 2021 Yangbi Foreshock-Mainshock Sequence, Yunnan, China: More than a Triggered Cascade

Yijian Zhou[1*], Chunmei Ren[2], Abhijit Ghosh[1], Haoran Meng[3], Lihua Fang[4*], Han Yue[2], Shiyong Zhou[2], Youjin Su[5]

[1]Department of Earth and Planetary Sciences, University of California, Riverside, California, USA

[2]Institute of Theoretical and Applied Geophysics, Peking University, Beijing, China.

[3]Southern University of Science and Technology, Guangdong, China

[4]Institute of Geophysics, China Earthquake Administration, Beijing, China

[5]Yunnan Earthquake Agency, Yunnan, China

Corresponding author:

Yijian Zhou (yijian.zhou@email.ucr.edu)

Lihua Fang (flh@cea-igp.ac.cn)

Key Points:

- The Yangbi mainshock and two smaller foreshocks occur on an unmapped near-vertical fault, and the largest foreshock occurs on a mapped stepover fault that dips to NE.
- The rupture directivity and source parameters of major foreshocks are estimated by aftershock distribution and spectral ratio analysis.
- The Yangbi sequence can be explained as a cascade sequence, but aseismic signals are also detected, including pre-slip cluster and afterslip migration.

Abstract

The 2021 M_w 6.1 Yangbi earthquake in southwest China is preceded by three major foreshocks: 05/18 M_w 4.3, 05/19 M_w 4.6, and 05/21 M_w 5.2. It provides a valuable chance to revisit two end-member models describing earthquake interaction: cascade-up and pre-slip model. We first determine the associated fault structure with relocated aftershocks and focal mechanisms obtained from multi-point-source inversion. We find that the mainshock and two smaller foreshocks occur on an unmapped near-vertical fault, and the largest foreshock occurs on a mapped stepover fault that dips to NE. Secondly, for each major foreshock, we estimate and delineate their rupture area based on aftershocks and spectral ratio analysis. Based on the rupture model, we finally calculate the evolution of Coulomb stress, with which to interpret the causality of each major event. Results show that the Yangbi sequence can be explained by the cascade triggering mechanism, while we also find evidence for aseismic slip that contributes to the triggering process: the first foreshock is preceded by a short-term localized cluster, and the aftershock zone of the second foreshock extents through time. The nucleation of mainshock is probably contributed by multiple major foreshocks through both seismic and aseismic processes. This detailed seismological characterization of Yangbi sequence lend supports for a deeper understanding on the foreshock mechanism: (1) the controlling mechanisms are not limited to cascade-up & pre-slip, multiple mechanisms can operate together; and (2) aseismic slip does not always provide more predictability on the mainshock.

Plain Language Summary

The 2021 M_w 6.1Yangbi earthquake is preceded by three M 4-5 earthquakes, which are known as foreshocks. Whether the foreshock sequence can lend predictability to the mainshock is of scientific interest. For the Yangbi foreshock sequence, we analyze the interaction between the major foreshocks with a high-resolution seismic catalog and the modeling of resulted stress transfer after each major foreshock. Results show that the Yangbi foreshock sequence is not helpful in the prediction of mainshock, but it deepens our understanding toward the phenomenon of foreshocks.

1. Introduction

Foreshocks are known as smaller earthquakes preceding the large mainshock (Jones and Molnar, 1979). Due to the neighboring location and temporal correlation, foreshocks are considered as a possible precursory phenomenon, e.g. the success prediction of 1975 M_w 7.0 Haicheng earthquake largely relies on the ~1-day foreshock activity (Wang et al., 2006). Traditionally, two end-member models are proposed to explain the triggering relationship between the foreshocks and mainshock (Dodge et al., 1996): the cascade model and the pre-slip model. The cascade model describes the seismic sequence as the cascade failure of isolated asperities, where each event is triggered by the stress transfer from the previous earthquake (Helmstetter et al., 2003; Felzer et al., 2004; Ellsworth and Bulut, 2018; Yoon et al., 2019). Thus, the initiation process of mainshock and foreshocks are identical, which lead to an unpredictable nature of the mainshock. On the other end, the pre-slip model regards the foreshocks as the byproduct of the nucleation process of the mainshock, where accelerating aseismic slip is accompanied. It is a deterministic model, because theoretical and laboratory studies have shown that the nucleation size, i.e. the area of pre-slip, scales with the final size of the mainshock (Dieterich, 1978; 1992; Ampuero and Rubin, 2008; Johnson et al., 2013). The different implications for earthquake predictability make it important to discriminate between different foreshock-mainshock triggering mechanisms.

The 2021 M_w 6.1 Yangbi earthquake that strikes the Yunnan province of southwest China is a typical large earthquake with prominent foreshock activity (Figure 1). It occurs near the southwestern boundary of Chuandian block (Zhang et al., 2003) dominated by right-lateral strike-slip motion (Shen et al., 2005). The aftershock of Yangbi earthquake reveals an NW-SE trending fault that is subparallel with the major active fault, i.e. Weixi-Qiaohou fault (Figure 1a). The Yangbi sequence is composed of the 21st May M_w 6.1 mainshock (denoted as *M*) and three major foreshocks (Figure 1b): the 18th May M_w 4.3 (*f1*), the 19th May M_w 4.6 (*f2*), and the 21st May M_w 5.2 earthquake (*F1*). Moment tensor inversion results in right-lateral focal mechanism for these four events (Yang et al., 2021), which is also consistent with the major fault trend. The foreshocks are located in the middle of the mainshock co-seismic fault segment, all of which show clear unilateral rupture, indicated by the relative location between the epicenter and their aftershocks (Figure 1b): *f1* and *f2* rupture to northwest, while *F1* mainly rupture to southeast with certain bilateral component.

Up to date, a few discussions are published on the triggering relation between those major foreshocks and the Yangbi mainshock, but no consistent conclusions are reached (e.g., Lei et al., 2021; Zhang et al., 2021; Liu et al., 2022; Sun et al., 2022). It is not surprising, since the conclusions on foreshock formation can vary by different analysis techniques and data conditions (Mignan, 2014). As an example, Ellsworth and Bulut (2018) made detailed event relocation and source spectra analysis to investigate the inter-event triggering effect of the 1999 Izmit foreshocks, which turned out to be a cascading sequence, instead of precursory aseismic slip loading proposed by Bouchon et al. (2011). Thus, the modeling of Coulomb stress with well-constraint event location and finite faulting model is necessary in such discussions. Fortunately, the rather dense regional seismic network in the Yunnan province of China made such analysis possible in Yangbi. Such well-recorded continental large earthquake with intense foreshock activity is rare, and thus provides a valuable chance to generate a well-depicted case for the seismological community. Moreover, the Yangbi earthquake is the largest event that occurs in southwest Chuandian block since the 1996 M_w 6.6 Lijiang earthquake (Han et al., 2004; Ji et al., 2017) and is the largest earthquake in China that has clear foreshock activity since the 1975 M_w 7.0 Haicheng earthquake (Xu et al., 1982; Wang et al., 2006). Thus, an in-depth study in the Yangbi sequence has implications on not only the foreshock mechanism and the seismic hazard of southwest China.

In this study, we follow a similar strategy as Ellsworth and Bulut (2018), but focus on larger events with finite source and rupture directivity, to investigate the triggering mechanism of Yangbi sequence. We first determine the local fault structure based on the rupture directivity, aftershock distribution, and the focal mechanism. Secondly, we delineate the finite rupture area for each major foreshock based on aftershocks and spectral ratio analysis. Finally, we model the evolution of Coulomb stress, based on which we interpret the causality of each major event.

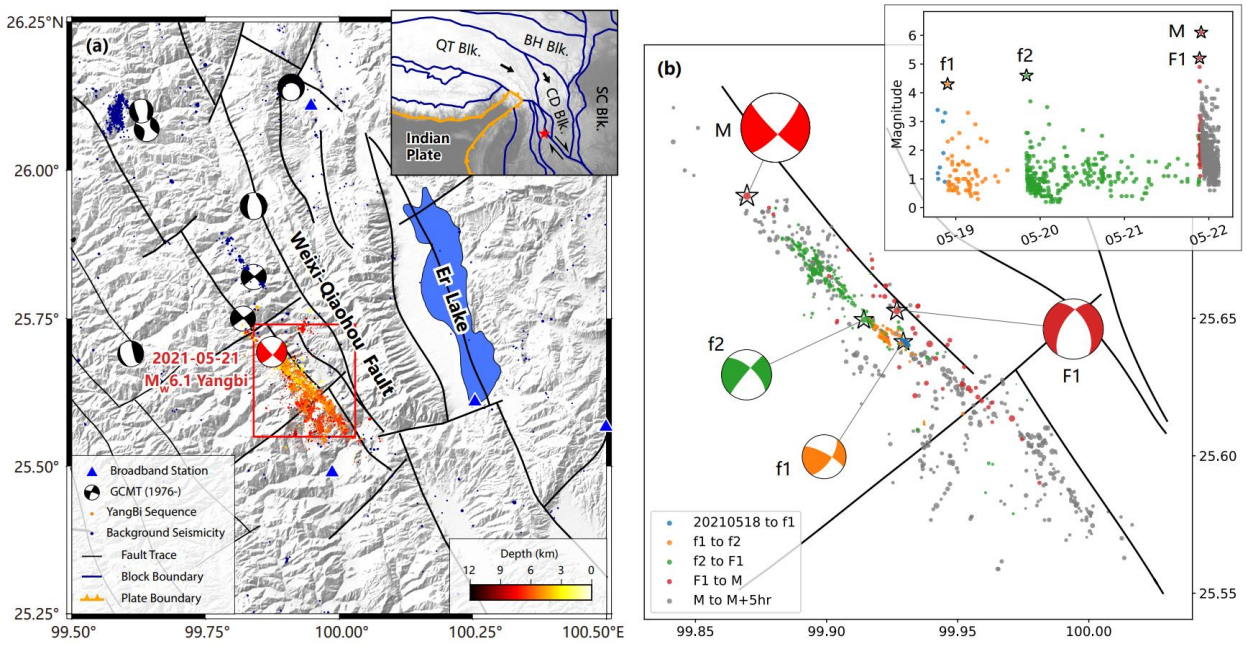

Figure 1. Tectonic background and foreshock sequence. (a) Tectonic background of the Yangbi earthquake. In the main plot, fault traces are plotted by black lines, and come from Wang et al. (2021). The interseismic background seismicity and Yangbi seismic sequence are plotted by blue and orange dots respectively, with the focal depth color-coded. Focal mechanism of GCMT since 1976 is plotted by black beachballs. Blue triangles mark the broadband stations. In the insert plot, the plate boundary and active block boundary are plotted by orange and blue lines, respectively. Main blocks, i.e. Qiangtang block (QT), Bayan Har block (BH), Chuandian block (CD), and South China block (SC), are noted, with their relative motion marked. (b) The Yangbi foreshock sequence. The study time period is divided by the major foreshocks (*f1*, *f2*, and *F1*) and the mainshock (*M*). Seismic catalog comes from Zhou et al. (2021a). The focal mechanisms of the mainshock and largest foreshocks are determined by multi-point-source inversion, and that of the first two smaller foreshocks comes from Yang et al. (2021).

2. Data and Methods

2.1 Seismic Catalog

We adopt a high-resolution seismic catalog constructed by Zhou et al. (2021a) with deep learning and matched filter. The catalog contains 7943 well-located events in the Yangbi source region from 2021-05-01 to 2021-05-28, which covers the foreshock and early-aftershock period that is interested in this study. The construction of this catalog utilized an AI-based phase picker to obtain the template catalog (Zhou et al., 2019) and matched filter to augment the templates (Zhou et al., 2021b). Such strategy gives reliable and highly complete detection, and thus the

catalog reaches a complete magnitude of M_L 1.0, and a minimum magnitude of M_L -1.0. The relocation process utilized cross-correlated differential travel times, which provides sub-sampling-rate precision (<0.01-s), leading to a relative location uncertainty of ~10m laterally and ~20m vertically in the hypoDD inversion process (Waldhauser, 2001; Zhou et al., 2021a).

2.2 Spectral Ratio Analysis

We use a spectral ratio method to extract the source spectrum of the Yangbi foreshocks, in the purpose of determining their rupture directivity and source parameters. This method utilizes empirical Green's function (EGF) to remove the wave propagation effect and site response in the target foreshock seismogram (Chen and Shearer, 2013; Ross and Ben-Zion, 2016; Ellsworth and Bulut, 2018; Yoon et al., 2019). EGFs are selected as smaller events (usually >1 magnitude smaller) that occur near the target event, so that they can be considered as point source and share similar ray paths with the target event. Thus, on the same station, the ratio between target and EGF spectra represents the source spectrum of target event, which contains the seismic source information, e.g. rupture area, coseismic slip, stress drop, etc. In the Yangbi sequence, we select the aftershocks of the target foreshock as EGF, which is both large enough to be clearly recorded on selected stations, and small enough to be considered as a point source. This leads to 6 to 10 EGFs with the magnitude range from M_L 2.6-3.5 for *f1* and *f2*, and M_L 2.9-4.1 for *F1*.

The rupture directivity can be revealed by the azimuthal variation of source spectrum (Calderoni et al., 2015; Calderoni et al., 2017). Based on the dynamic rupture theory, stations facing the rupture propagation direction are expected to observe a source-time function (STF) of shorter duration and higher amplitude; or, in the frequency domain, a higher corner frequency on the source spectrum (Haskell, 1964). Thus, we apply two sets of comparison on the source spectrum observed on two sides of the target earthquake: one set along fault-parallel direction and another along fault-normal direction. For unilateral rupture, the contrast of corner frequency along fault-parallel would be larger than the fault-normal one; for bilateral rupture, both directions have weak contrasts, but fault-parallel stations would record larger high-frequency components.

For the estimation of rupture area, we use fault-normal stations to obtain the corner frequency that has little directivity effect. We calculate the S-wave spectrum with a multi-taper algorithm (Prieto et al., 2009), and normalize it by its seismic moment (Ross and Ben-Zion, 2016). We adopt several strategies to improve the stability of spectral ratio calculation: (1) the initial

result is smoothed in log-scale by interpolation and sampling on every 0.025 of log(f); (2) for each event-station pair, we utilize a multi-window strategy (Imanishi and Ellsworth, 2006; Uchida et al., 2007; Yoon et al., 2019): three 10-s sliding windows with a 1.5-s stride are applied, where the first window starts from the S wave arrival. The spectrum of these sliding windows is averaged on the log scale; (3) the spectrum of different EGFs are stacked in the log-scale, since they have similar shape and amplitude (Ross and Ben-Zion, 2016). The final spectral ratio is obtained by dividing the target spectrum with the stacked EGF spectrum.

To estimate source parameters from spectral ratio, we first fit the omega-square source model proposed by Boatwright (1980) for the estimation of corner frequency:

$$\frac{u_1(f)}{u_2(f)} = \frac{M_{01}}{M_{02}} \sqrt{\frac{1+\left(\frac{f}{f_{c2}}\right)^4}{1+\left(\frac{f}{f_{c1}}\right)^4}}\ , \tag{1}$$

where sub-index 1 and 2 represent the target event and EGF, respectively; u is the spectrum, M_0 is the seismic moment, f_c is the corner frequency. Grid search of the moment ratio M_{01}/M_{02} and two corner frequency f_{c1} and f_{c2} is applied to fit the spectral ratio. In this process, the summed difference between predicted and observed spectral ratio on a frequency band of 0.2-20Hz is minimized in the logarithm scale. The source radius is estimated according to Madariaga (1976)'s theory, assuming a constant rupture velocity of $0.9v_s$:

$$r = \frac{0.21 v_s}{f_c}\ , \tag{2}$$

where v_s is the S wave velocity, which is set as 3.4-km/s, based on the local velocity structure (Liu et al., 2021). The average slip on the circular fault is thus:

$$D = \frac{M_0}{\mu \pi r^2}\ , \tag{3}$$

where μ is the shear modulus, and is set to 32 GPa. The static stress drop is estimated by Eshelby (1957)'s equation:

$$\Delta\sigma = \frac{7}{16}\frac{M_0}{r^3}\ . \tag{4}$$

2.3 Multi-Point-Source Moment Tensor Inversion

We adopt multi-point-source (MPS) inversion technique (Yue and Lay, 2020) to resolve the moment tensor of the largest foreshock and the mainshock. The MPS method utilize different subevents to model three-component broad-band records in the near field. It is primarily developed by (Kikuchi and Kanamori, 1982; 1986; 1991), and is improved by Yue and Lay (2020) with an iterative inversion algorithm. In this method, a priori constraints are set on the search time window of subevents, their potential location (mesh grids), and the shape of STF. The algorithm finally provides an estimation of the location, initiative time, focal mechanism, and moment of each subevent. This method has advantages for the largest foreshock of Yangbi, which is followed by two immediate aftershock that contaminate the tail wave (see Section 3.2). Thus, we want to refine the results obtained by gCAP method (e.g., Lei et al., 2021; Zhang et al., 2021). It is worth mentioning that polarity-based methods are not suitable as well, because of the imperfect station coverage and that most stations record upward polarity for *F1* (Figure S5-7).

To apply the MPS method in Yangbi, we first select 14 stations with epicentral distances between 30-160km for the largest foreshock, and 12 stations between 40-200km for the mainshock (Figure S9), considering the clipping effect of the nearest stations. All original waveforms are preprocessed by removing the instrumental response, band-pass filtering to 0.01-0.5Hz, and down-sampling to 10-Hz. Event waveforms are cut from 10-s before the initial P arrivals and ending with 130-s and 100-s time windows for foreshock and mainshock separately. For the computation of Green's function, we adopt the regional velocity model developed by joint-inversion of body and surface wave (Liu et al., 2021). The Green's function is computed with wavenumber-frequency integration algorithm (Zhu and Rivera, 2002) for each preset spatial grid. The spatial grids are distributed in a potential rupture area of about 15*6-km. For the largest foreshock and the mainshock, we respectively sliced 10*6 grids and 10*5 grids (Figure S10), considering the distribution of aftershocks. The selection of search time windows, i.e. window length and number of subevents, is based on the visual inspection on waveform and the inversion process (Text S1). For the largest foreshock, we used two subevents that occur between 0-5s and 5-10s; for the mainshock, we use three subevents during 0-3s, 5-8s, and 8-15s.

3. Results and Discussion

3.1 Rupture Directivity and Source Parameters of the Major Foreshocks

We first investigate the rupture directivity of the major foreshocks, since it is debatable in some published results (Lei et al., 2021; Zhang et al., 2021), and is essential in the determination of rupture area. As demonstrated in Section 2.2, we use the spectral ratio observed on different stations to determine the directivity. Based on the aftershock distribution and local fault traces (Figure 1b), we consider the major fault trend (SE-NW) as the possible rupture direction. Thus, we made two sets of comparisons along fault-normal and fault-parallel direction (Figure 2, and Figure S1a for adopted stations). It is obvious that the fault-parallel spectral ratios show more significant contrast, indicating that the rupture mainly occurs along the major fault trend, and that *f1* & *f2* rupture to the NW direction, while *F1* rupture to SE. This conclusion agrees with the relative location between the epicenter and aftershocks, but disagrees with Lei et al. (2021) that obtained a NE rupture for *F1* event, based on waveform fitting assuming different nodal planes. However, their waveform inversion utilized a 70-s time window for S wave, which is biased by two immediate large aftershocks (see next section), and there are no mapped NE-trending conjugate faults associated with *F1*, nor do its aftershocks distribute along that direction. Thus, our spectral ratio analysis determines that the Yangbi sequence is associated with faults that strike in NW-SE direction.

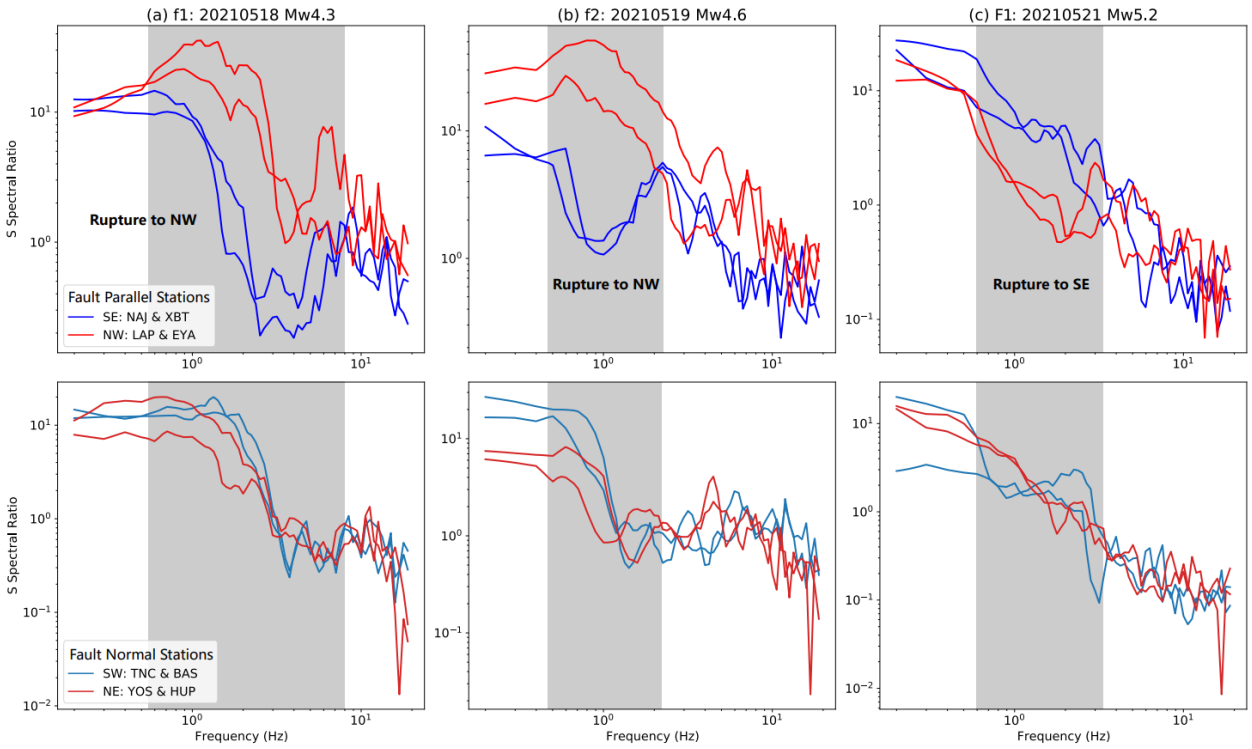

Figure 2. Spectral ratio comparison for directivity determination. (a), (b), and (c) plot the spectral ratio comparison of the foreshock *f1*, *f2*, and *F1*, respectively. The first and second line show the comparison along fault-parallel and fault-normal direction. Each line represents a spectral ratio observation on one station, with the color mark its azimuthal quadrant. The frequency bands with significant contrasts are highlighted by gray patches.

We then extract source parameters for these major foreshocks with fault-normal stations (Figure S1b), where directivity effect is minimized. The spectral ratios on different stations have consistent shape, and the resulting stacked spectral ratio is smooth, fitting well with the Boatwright model (Figure 3). The spectra fitting gives an estimation of corner frequency, which is directly related to the rupture area, assuming Madariaga (1976)'s dynamic model (Equ. 2): for *f1*, *f2* and *F1*, we got 3.25-km^2, 8.08-km^2, and 13.58-km^2, respectively. The amount of slip and stress drop are also estimated by combining the moment magnitude. We find that *f1* & *f2* have relatively low stress drop of ~1.0-MPa and a coseismic slip of 3-cm, while *F1* has ~3.5-MPa stress drop and ~16-cm coseismic slip (Figure 3).

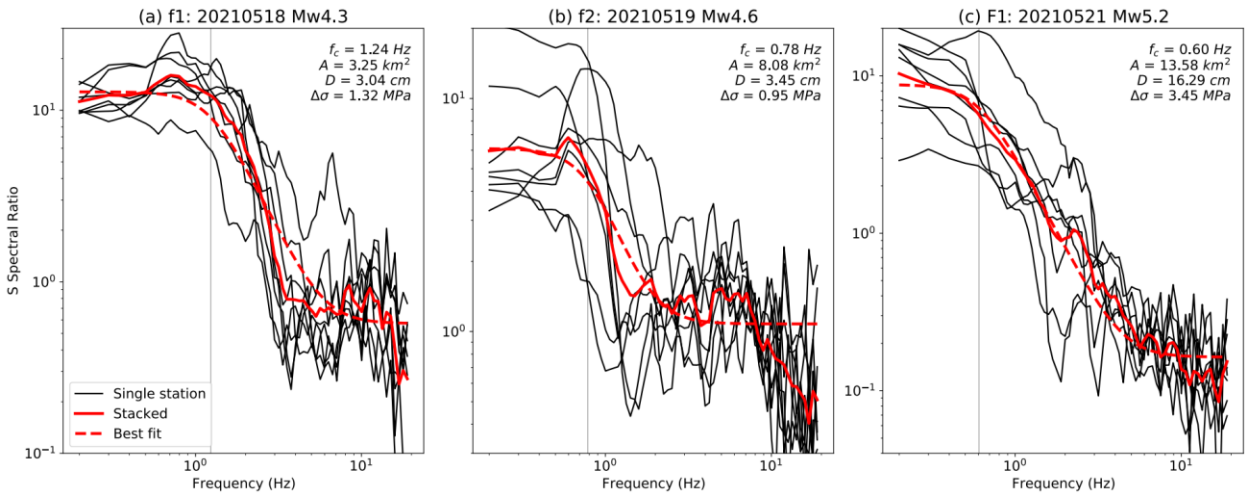

Figure 3. Spectral ratio analysis. (a), (b), and (c) plot the spectral ratio analysis of the foreshock *f1*, *f2*, and *F1*, respectively. The black lines, solid red lines, and dashed red lines denote the spectral ratio on single stations, stacked spectral ratio, and the best fit to Boatwright model to the stacked spectral ratio. The vertical gray line marks the estimated corner frequency.

3.2 Analysis of the Largest Foreshock

By inspecting the waveform of *F1*, we found that this largest foreshock of Yangbi is followed by two immediate aftershocks: M_w 4.9 *F2* and M_w 4.4 *F3* (Figure 4a). This raises challenges in the moment inversion process, since the waveform of different events are overlapped. Thus, as demonstrated in Section 2.3, we apply MPS inversion technique to *F1-3*, which is designed to resolve complex rupture process, and is not affected by overlapping waveforms. Results show that the largest foreshock *F1* is composed of two subevents (Figure 4b, Text S1), where the second and smaller subevent *F1_2* initiates after ~5-s, with its centroid locates at the NW of the first one. The temporal separation is significantly larger than the duration of an M ~5 earthquake, which probably indicates that *F1_1* and *F1_2* are two independent events that both rupture to SE. The summarized moment tensor of *F1* shows a ~60° NE dipping nodal plane and certain normal faulting component. This result is consistent with GCMT result, though our result show neglectable non-double-couple (NDC) component (Figure 4b). It is not surprising, since GCMT inverse long-window tele-seismic waveforms that represents an overall moment tensor including all three events, and that our MPS results show different dip angles between *F1-3*, which indicates geometrical complexity that can cause NDC in the summarized moment tensor (Julian et al., 1998).

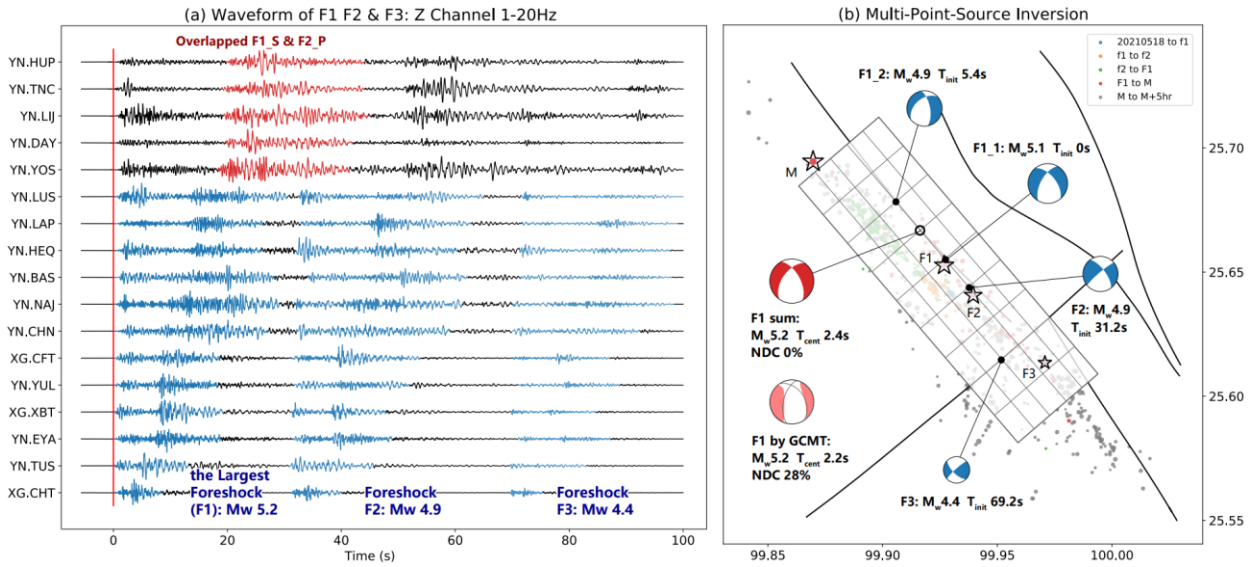

Figure 4. Multi-point-source (MPS) inversion for the largest foreshock (*F1*) and its two immediate aftershocks (*F2* & *F3*). (a) Waveform of *F1*, *F2*, and *F3*. The Z-channel waveform is band-pass filtered to 1-20Hz. The earthquake signal of *F1-3* are highlighted in blue. The relative remote stations with the S wave of F1 and P wave of F2 overlapped are marked in red. (b) The MPS inversion result of *F1-3*. The subevents of the whole sequence are marked in blue, with their centroid location distributed on the preset mesh grids. Note that *F1* is separated by two subevents, and the summarized moment tensor plot in red, with a comparison with that by GCMT plot in light-red.

The first immediate aftershock, i.e. *F2*, has a similarly large magnitude, thus may play an important role in triggering the mainshock, while is ignored by published results. We apply the spectral ratio analysis demonstrated in Section 2.2 to resolve its rupture source parameters. Note that the spectrum analysis is done with S-wave, which is less biased by the waveform of *F1*. We first examine the rupture directivity. The two-direction comparisons both show weak contrast in corner frequency, indicating bilateral rupturing (Figure 5a, b). However, the fault parallel stations observed pronounced high-frequency component (Figure 5a), suggesting that *F2* also rupture along the major fault trend. Thus, we adopt the fault-normal stations to extract its source parameters, as in the last section. We obtain a similarly large rupture area (~11 km^2), but a much smaller coseismic slip (~7 cm) and stress drop (~1.7 MPa).

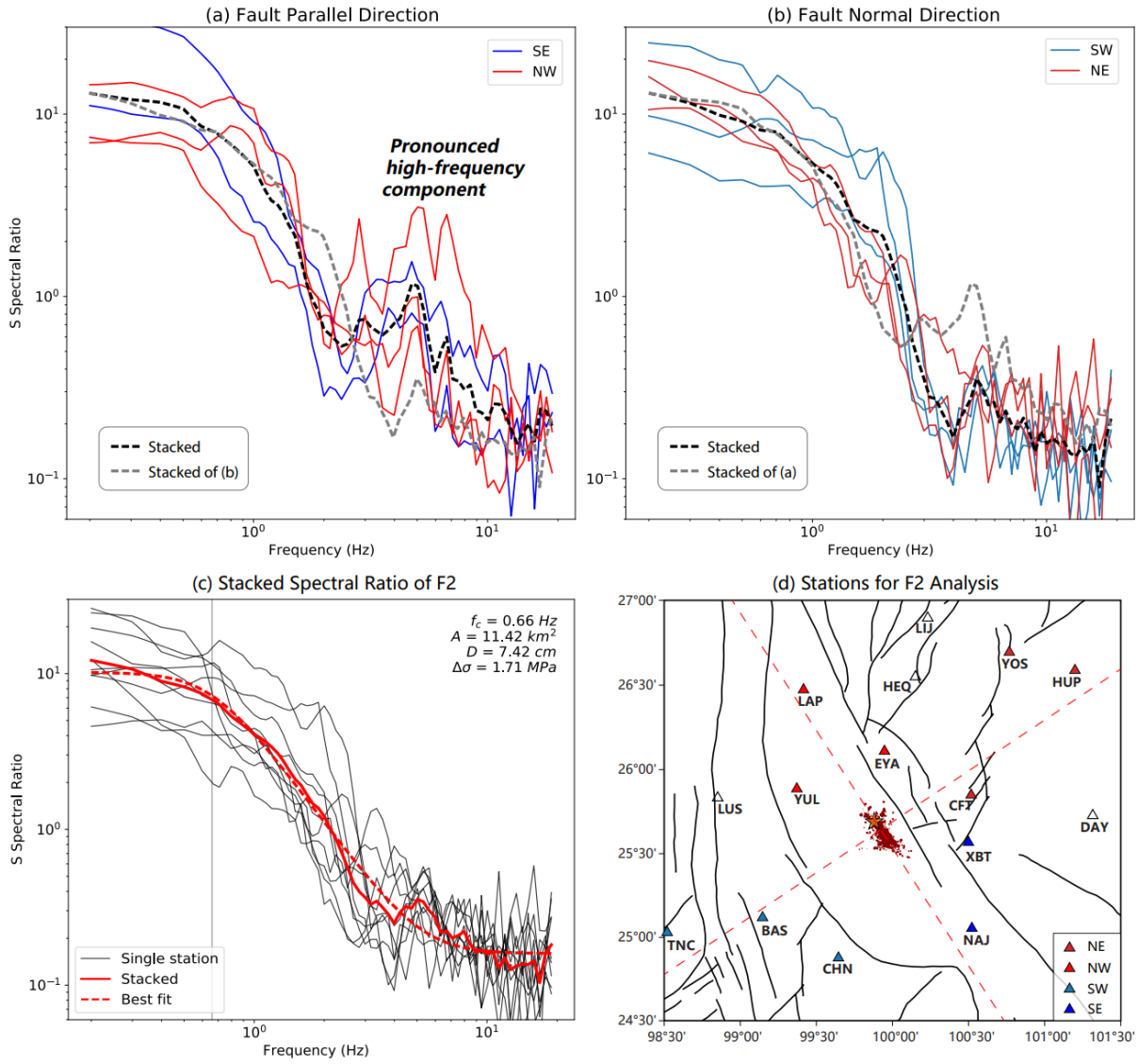

Figure 5. Spectral ratio analysis of *F2*. (a) & (b) are two sets of spectral ratio comparisons along fault-parallel and fault-normal direction, respectively. The dash lines are the stacked and averaged spectral ratio. (c) plots the stacked and fitted spectral ratio. The markers have the same meaning as in Figure 3. (d) shows the station distribution used in this analysis. Seismic stations are plotted in triangles, fault traces are plotted in black lines, and reference fault-parallel and fault-normal trend are marked by red dashed lines.

3.3 Construction of Fault Model

To prepare for the Coulomb stress calculation, we construct a fault model that delineates the local fault structure and rupture area of each major foreshock. The fault geometry is determined by the aftershock distribution, focal mechanism, and the mapped local fault traces. The local fault data show a clear left-lateral step-over feature (Figure 6a), and that the Yangbi mainshock and first

two smaller major foreshocks (*f1* & *f2*) are located off the mapped trace. However, the aftershocks on the NW of epicenter show a clear trend that connects to another mapped fault segment, indicating that the major fault is continuous at depth (Figure 6a). This fault segment associated with *M*, *f1*, and *f2* (denoted as *Fault_M*) is probably near-vertical, suggested by their focal mechanisms (Figure 1b, 6). The largest foreshock *F1* and its aftershocks are not on *Fault_M*, and are more likely to occur on the mapped segment (denoted as *Fault_F*), which is dipping to NE, as indicated by the focal mechanism (Figure 4b, 6a), the relative location between surface fault trace and microseismic events at depth (Figure 6a), and the aftershock distribution (cross-section CC' in Figure 7c). The dip angle of *Fault_F* is likely variable along strike, because the dip angle in the focal mechanisms of *F1* & *F2* are different, and that the aftershock trace is gradually merging with the surface fault trace (Figure 6). The two fault segments (*Fault_M* & *Fault_F*) intersect at the mapped stepover, where multiple unmapped conjugate faults are imaged by aftershocks, indicating geometrical complexity. This fault segment probably continues to SE at depth, while the surface trace alters to the mapped stepover, which is supported by the focal mechanism of *F3* and the third subevent of *M* that dip to SW (Figure 6). Though a connected fault makes rupture easier to propagate, the geometrical complexity causes the termination of mainshock rupture, as shown in our MPS inversion (Figure 6b) and other studies utilizing joint inversion of InSAR & GPS data (Li et al., 2022) or InSAR & seismic data (Wang et al., 2022).

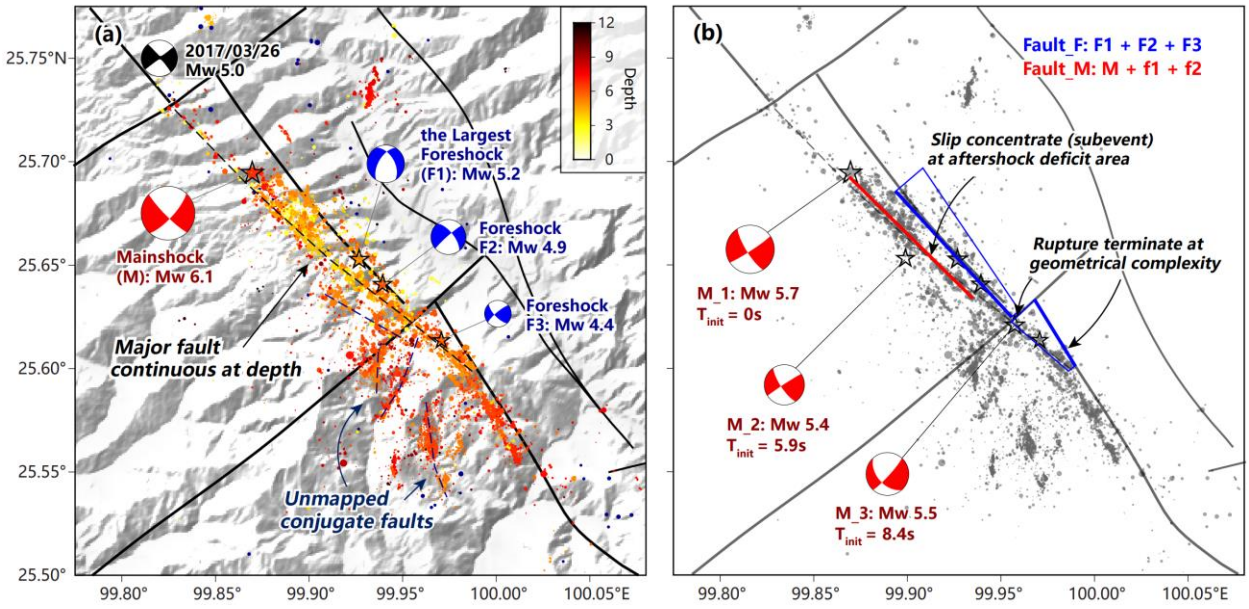

Figure 6. Fault geometry interpretation and MPS inversion of the mainshock. (a) Interpretation of fault geometry. The solid black lines are the mapped fault, the dashed black line is the unmapped major fault, and the dashed dark-blue lines are the unmapped conjugate faults. The blue beachballs mark the MPS-inversed focal mechanisms of the foreshock *F1-3*, and the hollow black stars mark their epicenters. (b) Simplified fault geometry and MPS inversion result of the mainshock. The solid red and blue line marks the simplified fault trace associated with the mainshock and the largest foreshock. The red beachballs mark the focal mechanisms of the mainshock subevents, and their centroid locations are marked by hollow stars.

The co-seismic rupture of major foreshocks is constrained jointly by aftershock distribution and spectrum-determined rupture area. As demonstrated in the last paragraph, the first two major foreshocks *f1* & *f2* occur on *Fault_M*, which is a near-vertical fault with pure right-lateral strike-slip events initiate on it. Their rupture area is well depicted by the aftershock distribution, because most of the aftershocks occur on only one side of the epicenter (Figure 7a), and that the extension of immediate aftershocks is rather clear (see Section 3.5). We draw a rectangular rupture area of *f1* & *f2* based on their immediate aftershocks (Figure 7a, b), which reach great consistency with the rupture area estimated with spectrum analysis in Section 3.1 (Figure 3a, b).

For the largest foreshock *F1*, we first simplify the *Fault_F* as a 60° NE dipping fault that slips with a rake angle of -150° (right-lateral + normal faulting), based on the focal mechanism solution. However, the coseismic rupture cannot be directly imaged from aftershocks, because the immediate aftershocks occur on both sides of the epicenter (though mainly on the SE size), and the total associated rectangular area is significantly larger than that inferred from spectral ratio method. Therefore, we adopt two end-member rupture models for *F1*, and show that this difference does not alter the interpretation of triggering relation (see Section 3.5), while only the preferred model and related Coulomb stress calculation is shown in the main text. The preferred model put the NW end of *F1* rupture on the location of the northernmost immediate aftershock, since the second subevent of *F1* locates on the NW of epicenter (Figure 4b). The southern end of *F1* rupture is set at the fault junction between the major fault and mapped conjugate fault (Figure 6a), which is also near the termination of the mainshock (*M_3*, Figure 6b). The top of *F1* rupture is set at 4-km, since the shallowest aftershock locates at 4-km, and that the shallower portion of the fault is probably near-vertical, so that the fault trace is separated at surface by the observed distance (see cross-section CC’ in Figure 7c). This preferred model leads to a rupture area consistent with the spectral ratio analysis (Figure 3c), and the overall rupture directivity is to SE, as shown in Figure

2c. Further evidence in support or against this model may come from source-time function extraction and subsequent subevent location technique with a rather dense seismic network (e.g., López-Comino and Cesca, 2018; Wu et al., 2019; Meng and Fan, 2021).

Another important event is the M_w 4.9 *F2*, i.e. the first and largest immediate aftershock of *F1*. As shown by spectrum analysis (see Section 3.2), *F2* is a bilateral rupture along *Fault_F* that has a similarly large rupture area as *F1*. Its rupture area is even harder to determine than *F1*, since we cannot decipher which aftershock is associated with *F2*. The best guess we can make is that *F2* ruptures a deeper portion (Figure 7b), which avoids an immediate re-rupturing of the same asperity. Again, further investigations would require near-source stations that can resolve the down-dip rupturing behavior. Based on the above reasons, we decide not to include *F2* in the Coulomb stress modeling, but will include it in our discussion in Section 3.5.

Our fault model of foreshocks forms a complementary pattern with the co-seismic rupture of the M_w 6.1 mainshock that concentrates at about 3-10km initially and propagates towards the shallower portion at SE side at about 2-6km (Li et al., 2022; Wang et al., 2022). This is a typical pattern for aftershock distribution and coseismic slip, as shown in many other case studies (e.g., Yue et al., 2017; Mendoza et al., 2019; Meng et al., 2021). Based on this model, we can calculate the static Coulomb stress change induced by each foreshock.

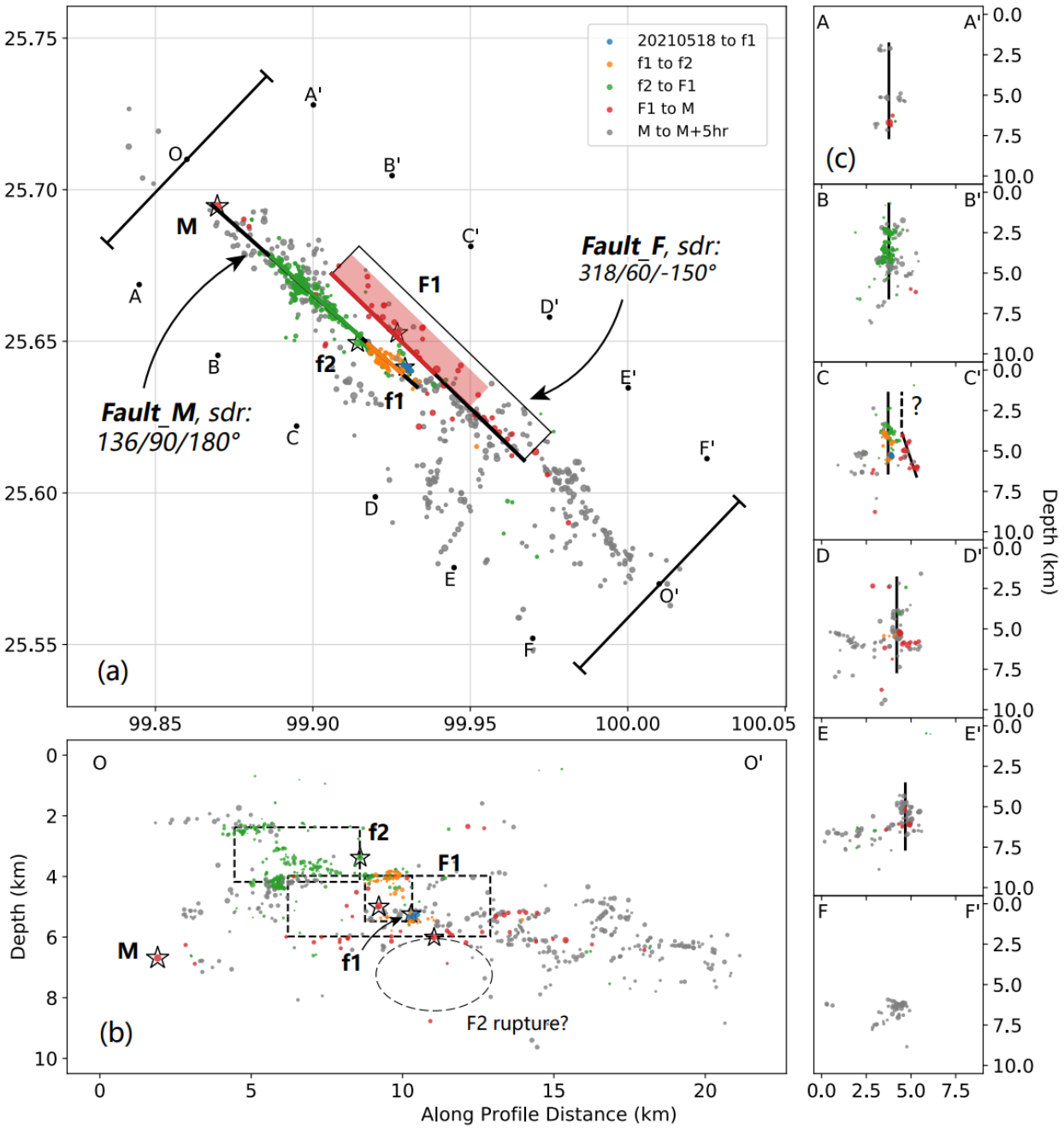

Figure 7. Distribution of seismic events and finite rupture model. (a) Map view, (b) cross-section along strike, and (c) fault-normal cross-sections. Events in different periods are denoted by colors. Four major foreshocks are marked by hollow stars. The simplified faults associated with the mainshock (*Fault_M*) and the largest foreshock (*Fault_F*) are denoted as thick black lines. The rupture length and area are marked by color line and patch in (a) and dashed black rectangles in (b).

3.4 Coulomb Stress Evolution

We calculate the static change of Coulomb failure stress (ΔCFS) with the Coulomb 3 software (Lin and Stein, 2004; Toda et al., 2005), which assumes a homogeneous elastic half-space. The fault patch and amount of slip are determined according to the previous section. The friction parameters are set as default: Coefficient of friction = 0.4, Poisson's ratio = 0.25, Young's modulus = $8*10^4$ MPa. We calculated the cumulated Coulomb stress change after each significant foreshock (Figure 8).

Results show that the foreshock *f1* causes a significant increase of ΔCFS near the hypocenter of *f2* (Figure 8a), indicating a cascade triggering. Note that *f1* also promotes the occurrence of *F1*, with a $\Delta CFS \approx 0.02 MPa$. Similarly, the foreshock *f2* causes positive ΔCFS on both *F1* and *M* as well (Figure 8b). For *F1*, the net effect of *f1* & *f2* caused a $\Delta CFS > 0.02 MPa$, which, though small, is above the traditionally considered threshold of 0.01-MPa for static triggering (e.g., Hardebeck et al., 1998; Ziv and Rubin, 2000; Parsons and Velasco, 2009). Note that the positive effect of *f2* on *Fault_F* rupturing is localized within 1-2km, which covers the separation of these two faults (Figure S17). The occurrence of *F1* pushes the 0.02-MPa ΔCFS boundary closer to the hypocenter of *M*, which is also true for another rupture model of *F1* that is purely unilateral towards SE (Figure S15-16). Again, this number is not significantly large compared with many statistical studies (e.g., King et al., 1994; Kilb et al., 2002), but is considered sufficient to explain the triggering in many other studies (Steacy et al., 2005, and references therein). More detailed discussions on the causality are presented in the next section.

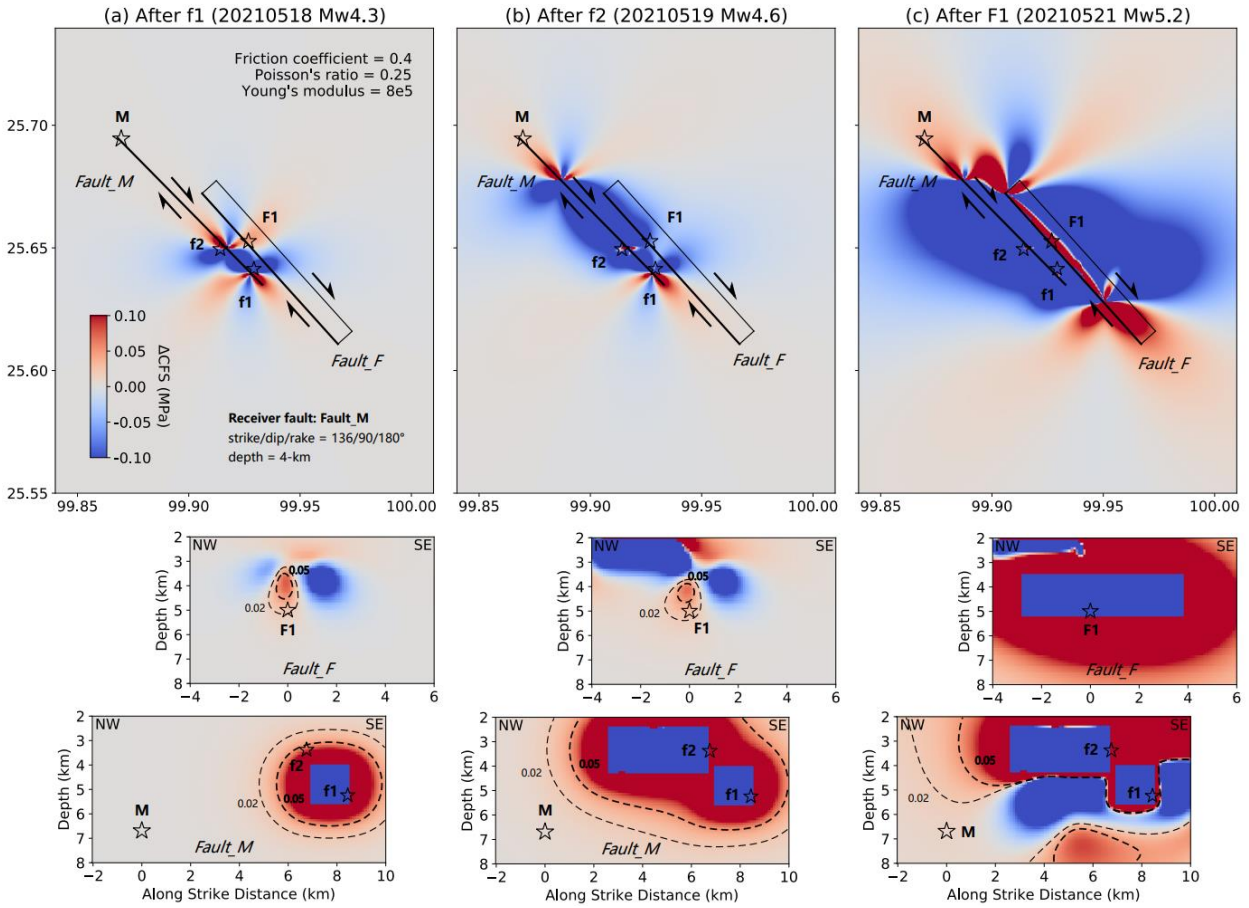

Figure 8. Evolution of Coulomb stress change. (a), (b), and (c) plot cumulated Coulomb stress change after *f1*, after *f2*, and after *F1*, respectively. The hypocenters are marked by stars. The upper and lower panels plot the map view with *Fault_M* as the receiver fault, and the cross-sections on *Fault_M* and *Fault_F*. Contours of 0.02-MPa and 0.05-MPa Coulomb stress increase are marked by dashed lines.

3.5 Interpretation of Inter-Event Triggering

3.5.1 How do the M_w 4.3 *f1* & M_w 4.6 *f2* initiate?

The initiation of *f1* is preceded by a micro-seismic swarm near the hypocenter (Figure 1b, 7a, 9a), probably indicating the nucleation process (Dieterich, 1992; Ampuero and Rubin, 2008). Similar highly clustered seismicity before a major earthquake is also observed in the 2019 M_w 6.4 Ridgecrest foreshock (Shelly, 2020) and the 2007 M_w 4.6 Odaesan, Korea, earthquake (Kim et al., 2010). This observation differs from Zhang et al. (2021) who claims no nucleation signal in Yangbi, but is consistent with the plots in Liu et al. (2022). It is clear in the fault-parallel profile that the asperity of *f1* is isolated from that of *f2* (Figure 7b, 9c), which explains why *f1* cannot rupture to a wider extent. The neighboring location of *f1* asperity & *f2* hypocenter and the large Coulomb stress

increase (Figure 8a) strongly indicate a cascade triggering mechanism. However, the static triggering theory cannot explain the time delay between events (Freed, 2005; Steacy et al., 2005). The ~20-hr time delay between *f1* and *f2* may be explained by further stress accumulation from afterslip or the nucleation process.

3.5.2 How does the M_w 5.2 *F1* initiate?

As demonstrated in Section 3.4, *f2* itself causes a >0.01-MPa Coulomb stress increase on the NW segment of *Fault_F* (Figure 8b, S17), which is sufficient to declare a static triggering effect. However, *f1* also plays a role in preparing for the initiation of *F1*, and the Coulomb stress increase is localized around the *F1* hypocenter (Figure 8a). Thus, it is probably *f1* that determines the hypocenter of *F1*. Another noticeable feature of the *f2*-induced ΔCFS is that it become negative above ~4-km, which is the lower boundary of *f2* rupture area. This may confine the *F1* hypocenter and its rupture area below 4-km, which is consistent with our setting of the fault model (Figure 7b, 9c). At the hypocentral depth of *F1* (~5-km), the positive effect of *f2* is more significant on the NW portion of *Fault_F* (Figure S17, 8b), which favors a second subevent on NW (as in Figure 4b), and that the rupture of *F1* is more likely has an extension to NW, instead of a purely SE-propagating unilateral rupture, as argued in Section 3.3.

While the static Coulomb stress change of *f1* & *f2* is sufficient to explain the occurrence of *F1*, we want to note here that some possible aseismic signals are also captured and may contribute to the triggering process. The aftershock zone of *f2* slightly expands along two sides of the coseismic rupture: ~1-km towards the NW side, and ~2-km to the SE side (Figure 9a). This migration of aftershock is probably driven by afterslip, a widely observed post-seismic relaxation phenomenon (Perfettini and Avouac, 2004; Kato, 2007; Barbot et al., 2009; Peng and Zhao, 2009; Meng and Peng, 2015). Note that the SE-propagating afterslip occurs on the area above *f1*, which would cause a positive Coulomb stress change on *F1*. Again, this mechanism can well explain the time delay between the occurrence of *f2* and *F1*. The possible afterslip towards NW will be discussed in the next subsection. Moreover, like *f1*, the largest foreshock *F1* is also preceded by an increasing occurrence of micro-seismic events near its hypocenter, though in a much shorter period and with much fewer events (Figure 9b). This swarm may imply the existence of pre-slip during nucleation or is a mini mainshock-aftershock sequence triggered by the afterslip of *f2*.

3.5.3 How does the M_w 6.1 *M* initiate?

Our Coulomb stress modeling shows that both *f2* and *F1* draw positive but relatively small ΔCFS on the mainshock hypocenter, but their summarized effect reaches a commonly adopted static triggering threshold of 0.01-MPa (Figure 8b, c). However, this may not be a satisfactory interpretation, since the short time interval between *F1* and *M* (~30-min) strongly indicates that the mainshock nucleation area has been critically stressed before *F1* or/and is significantly triggered by/after *F1*. Two other factors are likely incorporated in the triggering process: the afterslip of *f2* and the rupture of *F2*.

As pointed out in the last subsection, the aftershock zone of *f2* shows an expansion towards both sides along *Fault_M*, indicating an afterslip migration. The NW migrating afterslip would cause a positive Coulomb stress change on *M*, driving it closer to failure. Based on the aftershock evolution (Figure 9a), the average migration velocity can be estimated as 1.4-km/d, if we assume that the mainshock is initiated immediately when the creep front reaches its epicenter. It is also possible that the afterslip zone does not completely fill the gap between *f2* rupture and *M*, since a ~1.5-km gap on the NW is not filled by migrated aftershocks (Figure 9a). However, the magnitude of *f2* is too small (M_w 4.6) to generate visible afterslip for GPS, thus makes it difficult to validate the existence and extension of afterslip. Though no direct evidence in Yangbi, afterslip generated by M 4-5 or even smaller earthquakes have been observed in California with borehole strain data, and they tend to release a higher ratio of coseismic moment compared with that of large earthquakes (Hawthorne et al., 2016; Alwahedi and Hawthorne, 2019). If the *Fault_M* is already critically stressed before *F1*, it would be susceptible to small static stress change or even dynamic stress of F1 (Freed, 2005; Yun et al., 2019).

We point out in Section 3.3 that the rupture area of *F2* is hard to determine, which prevents us from obtaining an accurate ΔCFS modeling. However, *F2* has a comparable magnitude (M_w 4.9) as the largest foreshock *F1*, and the NW end of its rupture area probably reaches near the *F1* epicenter (Figure 7b, 9c), which suggests a non-negligible triggering effect. Similar to the ΔCFS by pure-unilateral *F1* rupture model (Figure S16), we suspect that *F2* could cause a 0.01-0.02MPa Coulomb stress increase, which is comparably large as the contribution from *F1*.

Thus, the occurrence of Yangbi mainshock is probably a joint result of multiple major foreshocks that combines both seismic and aseismic process. It becomes the mainshock by chance, because its hypocenter is not the first to nucleate, or those major foreshocks would likely become

its aftershock, or part of its rupture process. Such unpredictable feature fit better with the cascade model demonstrated in the Introduction (Helmstetter et al., 2003; Felzer et al., 2004; Ellsworth and Bulut, 2018; Yoon et al., 2019).

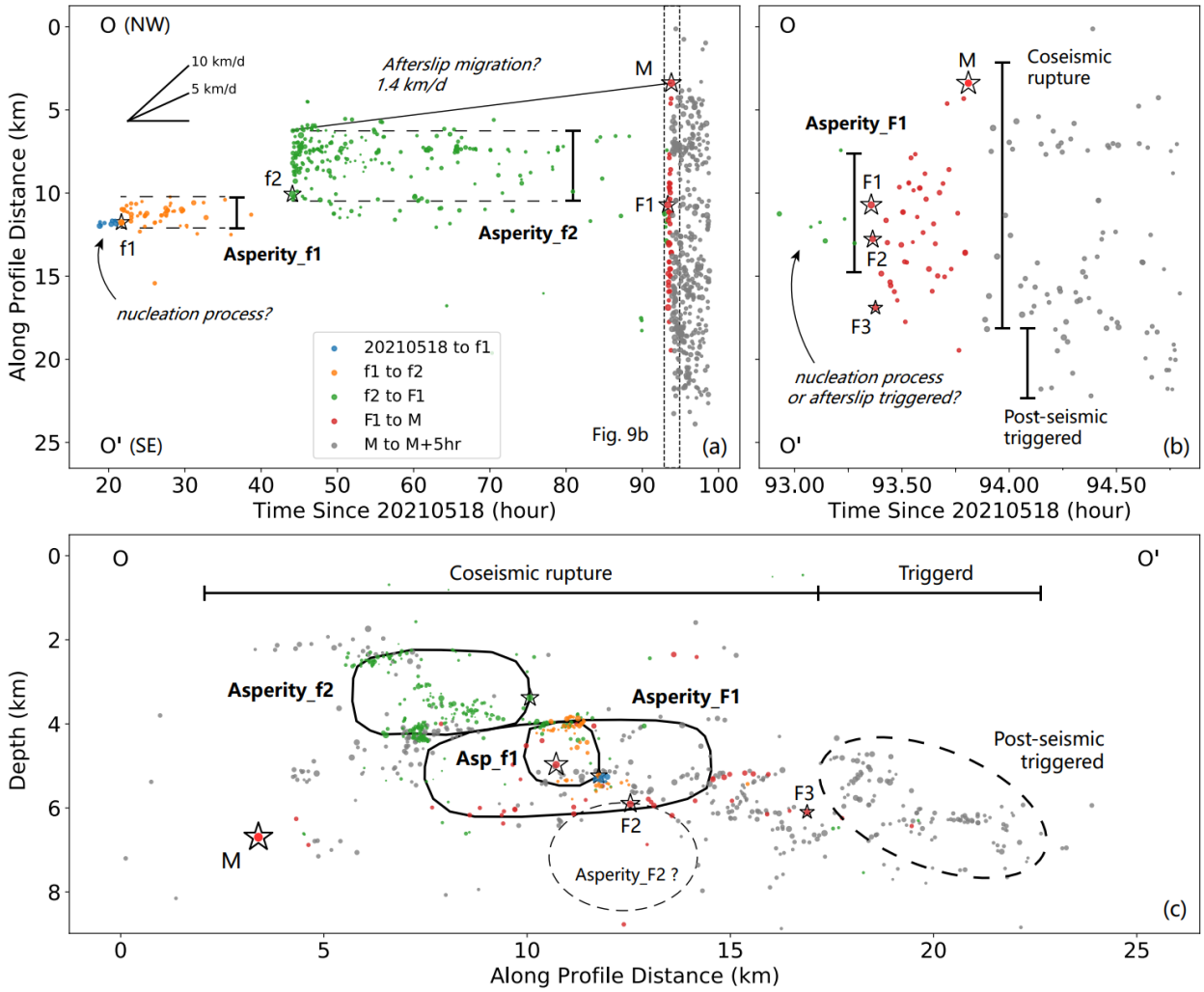

Figure 9. Migration pattern and interpretation of triggering mechanism. (a) and (b) plot seismicity migration along strike. The reference points OO' are the same as in Figure 7. The extension of different asperities is marked by vertical lines. (c) plot fault-parallel cross-section, with the rough boundary of asperity delineated by solid lines.

3.5.4 Comparison with Published Results

As discussed in previous subsections, we find that Yangbi sequence is basically a cascade sequence, while aseismic signals probably exist and play an important role in the triggering process.

However, many published studies reach different conclusions. Here, we provide a brief review and comparisons on those results.

Similar as our conclusion, the cascade model is preferred by Zhang et al. (2021) and Liu et al. (2022), both of which point out that the major foreshocks occur in a random behavior, and there is no consistent migration direction. However, Zhang et al. (2021) argues that no aseismic signals can be found, e.g. repeaters, while Liu et al. (2022) argues that *F1* is triggered by aseismic slip based on the fact that *f1* & *f2* cause negative Coulomb stress change. We consider both of the arguments have certain flaw: (1) we do observe some indicators for aseismic slip, e.g. the pre-event cluster in *f1* and the aftershock zone expansion in *f2* (see Section 3.5); (2) the negative ΔCFS resulted in Liu et al. (2022) is caused by an inaccurate event location and rupture model (see Section 3.4).

Tidal triggering is proposed by Lei et al. (2021), who reaches this conclusion because the major events coincide with the peak values of tidal strain and tidal shear & normal stress. However, this inference is not rigorous, since (1) the triggering effect should be decided on Coulomb stress, instead of strain, shear, or normal stress, and that those major events initiate at times of near-zero or even negative tidal-induced Coulomb stress change; (2) the tidal effect causes too small stress change, which is 2-orders smaller than coseismic stress transfer. Thus, we disagree that the observations in Lei et al. (2021) can indicate tidal triggering.

The tidal sensitive observation given by Lei et al. (2021) lead to another deduction that fluid plays an important role in the Yangbi sequence, which is supported by Sun et al. (2022), who detected an area of high V_P/V_S ratio at about 18-30km beneath the Yangbi sequence. However, both studies show no direct evidence for the existence of fluids and fluid upwelling, and the seismicity pattern in Yangbi is very different from that driven by fluid, e.g. 2009 L'Aquila sequence, where the seismicity migrates along a consistent direction and follows the fluid diffusion law (Di Luccio et al., 2010; Chiaraluce et al., 2011; Cabrera et al., 2022). Further investigations on the existence and effects of fluid may include extracting time-dependent V_P/V_S pattern (e.g., Di Luccio et al., 2010; Lin, 2020), long-term search for fluid-driven seismicity migration, and statistical analysis of source parameters (e.g., stress drop, Cabrera et al., 2022).

3.6 Implications on Foreshock Triggering Modes

As reviewed in the Introduction, cascade-up and pre-slip model are two end-member models for foreshock mechanism. However, with accumulating observational studies, the understanding becomes more complicated:

(1) The inter-event triggering in cascade model can be realized through aseismic slip as well, i.e. the afterslip of large foreshocks. For example, the 2016 M_w 7.0 Kumamoto earthquake is triggered by both the static stress change and the afterslip of M_w 6.2 foreshock (Kato et al., 2016). However, the inclusion of aseismic slip does not help predict the initiation time and size of the mainshock, which is similar as what we observed in Yangbi.

(2) Slow-slip events can be an external driven source that triggers both the foreshock and the mainshock. This kind of triggering mechanism is also widely observed, e.g. the 2011 M_w 9.0 Tohoku (Kato et al., 2012), the 2014 M_w 8.1 Iquique (Kato and Nakagawa, 2014; Ruiz et al., 2014), and the 2017 M_w 6.9 Valparaiso earthquake (Ruiz et al., 2017). Again, the aseismic slip in such mechanism does not provide predictability on the magnitude of mainshock, but the migration direction of foreshock sequence does give a clue of where the mainshock may occur. This mechanism serves as another mode besides cascading and pre-slip model, and thus implies that only searching for aseismic-slip-indicators is not enough in the discrimination of foreshock triggering modes.

(3) For the pre-slip nucleation phase, we still lack direct observations in the field. Near field observations with bore-hole strain meter have reported no similar nucleation signals so far (Roeloffs, 2006), even before the 2004 Parkfield earthquake (Johnston et al., 2006). Meng and Fan (2021) detect immediate foreshocks in the 2019 Ridgecrest aftershocks, but found that they follow mostly the cascade mode, with no scaling between the characteristic of their P wave and the magnitude of target event. Though Tape et al. (2018) reports possible nucleation signals in the strike-slip fault system in central Alaska, it comes in the form of very-low-frequency earthquakes, instead of significant foreshocks. It may be interesting to perform large-scale statistics on the candidate pre-slip clusters like that preceding *f1* in our study.

(4) Multiple mechanisms can coexist in a foreshock-mainshock sequence. Based on recent laboratory observations, McLaskey (2019) proposes a rate-dependent cascade-up model that includes contributions from both cascade-up and pre-slip mechanism. Case studies have also indicated such dual-mode mechanism in foreshock sequences, e.g. the 2009 M_w 6.3 L'Aquila

earthquake (Cabrera et al., 2022), the 2010 M_w 7.2 El-Mayor earthquake (Yao et al., 2020), and the 2019 M_w 7.1 Ridgecrest earthquake (Huang et al., 2020; Yue et al., 2021).

4. Conclusions

In this paper, we utilize seismological methods to characterize the 2021 Yangbi foreshock sequence, in the purpose of analyzing the causality between the major events. We find that the Yangbi sequence is associated with a rather complex fault geometry, with the mainshock and two smaller foreshocks occur on an unmapped near-vertical fault, and the largest foreshock occurs on a mapped stepover fault that dips to NE. The geometrical complexity confines the rupture extension of the mainshock and some foreshocks. Coulomb stress modeling shows that the foreshock triggering process can be explained by cascade triggering, while we also find evidence for aseismic slip that contributes to the triggering process. We conclude that the nucleation of mainshock is the result of multiple major foreshocks with both seismic and aseismic process, and that the formation of this foreshock-mainshock sequence is probably a coincidence. This detailed observation lend supports to the developed understanding on foreshock triggering mechanism: (1) the foreshock model is not limited to cascade-up & pre-slip, multiple mechanisms can operate together; and (2) aseismic slip does not always provide more predictability on the mainshock.

Acknowledgments

We thank the Yunnan Earthquake Agency for providing the continuous seismic data; Prof. Zhonghai Wu for sharing the local fault trace data; Dr. Baoning Wu, Prof. Zhigang Peng, and Prof. Daoyuan Sun for valuable suggestions in preparing the paper. Figures in this paper are plotted with Matplotlib and GMT. The python implementation of multi-taper method (Prieto et al., 2009) is available at https://github.com/krischer/mtspec. The Coulomb-3 software is available at https://www.usgs.gov/node/279387. This research is supported jointly by the National Key R&D Program of China (2021YFC3000702), the Nature Science Foundation of China projects (grants no. U2139205 & U2039204), US National Science Foundation (award number 1941719).

Data Availability

Seismic catalog used in this paper is available on Github: https://doi.org/10.5281/zenodo.5548377 (https://github.com/YijianZhou/Seismic-Catalog/blob/main/zhou_eqs-2021_Yangbi_pal-cerp-mess.ctlg).

References

Alwahedi, M. A., and J. C. Hawthorne (2019). Intermediate-Magnitude Postseismic Slip Follows Intermediate-Magnitude (M 4 to 5) Earthquakes in California, *Geophysical Research Letters*, *46*(7), 3676-3687, doi:https://doi.org/10.1029/2018GL081001.

Ampuero, J.-P., and A. M. Rubin (2008). Earthquake nucleation on rate and state faults – Aging and slip laws, *Journal of Geophysical Research: Solid Earth*, *113*(B1), doi:https://doi.org/10.1029/2007JB005082.

Barbot, S., Y. Fialko, and Y. Bock (2009). Postseismic deformation due to the Mw 6.0 2004 Parkfield earthquake: Stress-driven creep on a fault with spatially variable rate-and-state friction parameters, *Journal of Geophysical Research: Solid Earth*, *114*(B7), doi:https://doi.org/10.1029/2008JB005748.

Boatwright, J. (1980). A spectral theory for circular seismic sources; simple estimates of source dimension, dynamic stress drop, and radiated seismic energy, *Bulletin of the Seismological Society of America*, *70*(1), 1-27, doi:10.1785/bssa0700010001.

Bouchon, M., H. Karabulut, M. Aktar, S. Özalaybey, J. Schmittbuhl, and M.-P. Bouin (2011). Extended Nucleation of the 1999 Mw7.6 Izmit Earthquake, *Science*, *331*(6019), 877-880, doi:10.1126/science.1197341.

Cabrera, L., P. Poli, and W. B. Frank (2022). Tracking the Spatio-Temporal Evolution of Foreshocks Preceding the Mw 6.1 2009 L'Aquila Earthquake, *Journal of Geophysical Research: Solid Earth*, *127*(3), e2021JB023888, doi:https://doi.org/10.1029/2021JB023888.

Calderoni, G., A. Rovelli, Y. Ben-Zion, and R. Di Giovambattista (2015). Along-strike rupture directivity of earthquakes of the 2009 L'Aquila, central Italy, seismic sequence, *Geophysical Journal International*, *203*(1), 399-415, doi:10.1093/gji/ggv275.

Calderoni, G., A. Rovelli, and R. Di Giovambattista (2017). Rupture Directivity of the Strongest 2016–2017 Central Italy Earthquakes, *Journal of Geophysical Research: Solid Earth*, *122*(11), 9118-9131, doi:https://doi.org/10.1002/2017JB014118.

Chen, X., and P. M. Shearer (2013). California foreshock sequences suggest aseismic triggering process, *Geophysical Research Letters*, *40*(11), 2602-2607, doi:https://doi.org/10.1002/grl.50444.

Chiaraluce, L., L. Valoroso, D. Piccinini, R. Di Stefano, and P. De Gori (2011). The anatomy of the 2009 L'Aquila normal fault system (central Italy) imaged by high resolution foreshock and aftershock locations, *Journal of Geophysical Research: Solid Earth*, *116*(B12), doi:https://doi.org/10.1029/2011JB008352.

Di Luccio, F., G. Ventura, R. Di Giovambattista, A. Piscini, and F. R. Cinti (2010). Normal faults and thrusts reactivated by deep fluids: The 6 April 2009 Mw 6.3 L'Aquila earthquake, central Italy, *Journal of Geophysical Research: Solid Earth*, *115*(B6), doi:https://doi.org/10.1029/2009JB007190.

Dieterich, J. H. (1978). Preseismic fault slip and earthquake prediction, *Journal of Geophysical Research: Solid Earth*, *83*(B8), 3940-3948, doi:https://doi.org/10.1029/JB083iB08p03940.

Dieterich, J. H. (1992). Earthquake nucleation on faults with rate-and state-dependent strength, *Tectonophysics*, *211*(1), 115-134, doi:https://doi.org/10.1016/0040-1951(92)90055-B.

Dodge, D. A., G. C. Beroza, and W. L. Ellsworth (1996). Detailed observations of California foreshock sequences: Implications for the earthquake initiation process, *Journal of*

601 *Geophysical Research: Solid Earth*, *101*(B10), 22371-22392,
602 doi:https://doi.org/10.1029/96JB02269.
603 Ellsworth, W. L., and F. Bulut (2018). Nucleation of the 1999 Izmit earthquake by a triggered
604 cascade of foreshocks, *Nature Geoscience*, *11*(7), 531-535, doi:10.1038/s41561-018-0145-
605 1.
606 Eshelby, J. D. (1957). The determination of the elastic field of an ellipsoidal inclusion, and related
607 problems, *Proceedings of the Royal Society of London. Series A. Mathematical and*
608 *Physical Sciences*, *241*(1226), 376-396, doi:doi:10.1098/rspa.1957.0133.
609 Felzer, K. R., R. E. Abercrombie, and G. r. Ekström (2004). A Common Origin for Aftershocks,
610 Foreshocks, and Multiplets, *Bulletin of the Seismological Society of America*, *94*(1), 88-98,
611 doi:10.1785/0120030069.
612 Freed, A. M. (2005). Earthquake Triggering by Static, Dynamic, and Postseismic Stress Transfer,
613 *Annual Review of Earth and Planetary Sciences*, *33*(1), 335-367,
614 doi:10.1146/annurev.earth.33.092203.122505.
615 Han, Z.-j., S.-m. Guo, H.-f. Xiang, J.-s. Zhang, and Y.-k. Ran (2004). Seismotectonic environment
616 of occurring the February 3, 1996 Lijiang M=7.0 earthquake, Yunnan province, *Acta*
617 *Seismologica Sinica*, *17*(4), 453-463, doi:10.1007/s11589-004-0025-1.
618 Hardebeck, J. L., J. J. Nazareth, and E. Hauksson (1998). The static stress change triggering model:
619 Constraints from two southern California aftershock sequences, *Journal of Geophysical*
620 *Research: Solid Earth*, *103*(B10), 24427-24437, doi:https://doi.org/10.1029/98JB00573.
621 Haskell, N. A. (1964). Total energy and energy spectral density of elastic wave radiation from
622 propagating faults, *Bulletin of the Seismological Society of America*, *54*(6A), 1811-1841,
623 doi:10.1785/bssa05406a1811.
624 Hawthorne, J. C., M. Simons, and J.-P. Ampuero (2016). Estimates of aseismic slip associated
625 with small earthquakes near San Juan Bautista, CA, *Journal of Geophysical Research:*
626 *Solid Earth*, *121*(11), 8254-8275, doi:https://doi.org/10.1002/2016JB013120.
627 Helmstetter, A., D. Sornette, and J.-R. Grasso (2003). Mainshocks are aftershocks of conditional
628 foreshocks: How do foreshock statistical properties emerge from aftershock laws, *Journal*
629 *of Geophysical Research: Solid Earth*, *108*(B1),
630 doi:https://doi.org/10.1029/2002JB001991.
631 Huang, H., L. Meng, R. Bürgmann, W. Wang, and K. Wang (2020). Spatio-temporal foreshock
632 evolution of the 2019 M 6.4 and M 7.1 Ridgecrest, California earthquakes, *Earth and*
633 *Planetary Science Letters*, *551*, 116582, doi:https://doi.org/10.1016/j.epsl.2020.116582.
634 Imanishi, K., and W. L. Ellsworth (2006). Source Scaling Relationships of Microearthquakes at
635 Parkfield, CA, Determined Using the SAFOD Pilot Hole Seismic Array, in *Earthquakes:*
636 *Radiated Energy and the Physics of Faulting*, edited, pp. 81-90,
637 doi:https://doi.org/10.1029/170GM10.
638 Ji, L., Q. Wang, J. Xu, and J. Feng (2017). The 1996 Mw 6.6 Lijiang earthquake: Application of
639 JERS-1 SAR interferometry on a typical normal-faulting event in the northwestern Yunnan
640 rift zone, SW China, *Journal of Asian Earth Sciences*, *146*, 221-232,
641 doi:https://doi.org/10.1016/j.jseaes.2017.05.029.
642 Johnson, P. A., B. Ferdowsi, B. M. Kaproth, M. Scuderi, M. Griffa, J. Carmeliet, R. A. Guyer, P.-
643 Y. Le Bas, D. T. Trugman, and C. Marone (2013). Acoustic emission and microslip
644 precursors to stick-slip failure in sheared granular material, *Geophysical Research Letters*,
645 *40*(21), 5627-5631, doi:https://doi.org/10.1002/2013GL057848.

Johnston, M. J. S., R. D. Borcherdt, A. T. Linde, and M. T. Gladwin (2006). Continuous Borehole Strain and Pore Pressure in the Near Field of the 28 September 2004 M 6.0 Parkfield, California, Earthquake: Implications for Nucleation, Fault Response, Earthquake Prediction, and Tremor, *Bulletin of the Seismological Society of America*, *96*(4B), S56-S72, doi:10.1785/0120050822.

Jones, L. M., and P. Molnar (1979). Some characteristics of foreshocks and their possible relationship to earthquake prediction and premonitory slip on faults, *Journal of Geophysical Research: Solid Earth*, *84*(B7), 3596-3608, doi:https://doi.org/10.1029/JB084iB07p03596.

Julian, B. R., A. D. Miller, and G. R. Foulger (1998). Non-double-couple earthquakes 1. Theory, *Reviews of Geophysics*, *36*(4), 525-549, doi:https://doi.org/10.1029/98RG00716.

Kato, A., K. Obara, T. Igarashi, H. Tsuruoka, S. Nakagawa, and N. Hirata (2012). Propagation of Slow Slip Leading Up to the 2011 Mw9.0 Tohoku-Oki Earthquake, *Science*, *335*(6069), 705-708, doi:10.1126/science.1215141.

Kato, A., and S. Nakagawa (2014). Multiple slow-slip events during a foreshock sequence of the 2014 Iquique, Chile Mw 8.1 earthquake, *Geophysical Research Letters*, *41*(15), 5420-5427, doi:https://doi.org/10.1002/2014GL061138.

Kato, A., J. i. Fukuda, S. Nakagawa, and K. Obara (2016). Foreshock migration preceding the 2016 Mw 7.0 Kumamoto earthquake, Japan, *Geophysical Research Letters*, *43*(17), 8945-8953, doi:https://doi.org/10.1002/2016GL070079.

Kato, N. (2007). Expansion of aftershock areas caused by propagating post-seismic sliding, *Geophysical Journal International*, *168*(2), 797-808, doi:10.1111/j.1365-246X.2006.03255.x.

Kikuchi, M., and H. Kanamori (1982). Inversion of complex body waves, *Bulletin of the Seismological Society of America*, *72*(2), 491-506, doi:10.1785/bssa0720020491.

Kikuchi, M., and H. Kanamori (1986). Inversion of complex body waves-II, *Physics of the Earth and Planetary Interiors*, *43*(3), 205-222, doi:https://doi.org/10.1016/0031-9201(86)90048-8.

Kikuchi, M., and H. Kanamori (1991). Inversion of complex body waves—III, *Bulletin of the Seismological Society of America*, *81*(6), 2335-2350, doi:10.1785/bssa0810062335.

Kilb, D., J. Gomberg, and P. Bodin (2002). Aftershock triggering by complete Coulomb stress changes, *Journal of Geophysical Research: Solid Earth*, *107*(B4), ESE 2-1-ESE 2-14, doi:https://doi.org/10.1029/2001JB000202.

Kim, W.-Y., H. Choi, and M. Noh (2010). The 20 January 2007 Odaesan, Korea, Earthquake Sequence: Reactivation of a Buried Strike-Slip Fault?, *Bulletin of the Seismological Society of America*, *100*(3), 1120-1137, doi:10.1785/0120090069.

King, G. C. P., R. S. Stein, and J. Lin (1994). Static stress changes and the triggering of earthquakes, *Bulletin of the Seismological Society of America*, *84*(3), 935-953, doi:10.1785/bssa0840030935.

Lei, X., Z. Wang, S. Ma, and C. He (2021). A preliminary study on the characteristics and mechanism of the May 2021 M_S6.4 Yangbi earthquake sequence，Yunnan，China, *Acta Seismologica Sinica*, *43*(3), 261, doi:10.11939/jass.20210100.

Li, C., X. Shan, G. Zhang, C. Zhao, W. Gong, and Y. Zhang (2022). Slip Kinematics of the 2021 Yangbi Earthquake: Fore-Main-Aftershock Sequence Rupture along an Unknown Secondary Fault of the Weixi–Qiaohou Fault, *Seismological Research Letters*, doi:10.1785/0220210220.

692 Lin, G. (2020). Spatiotemporal variations of in situ Vp/Vs ratio within the Salton Sea Geothermal
693 Field, southern California, *Geothermics*, *84*, 101740,
694 doi:https://doi.org/10.1016/j.geothermics.2019.101740.
695 Lin, J., and R. S. Stein (2004). Stress triggering in thrust and subduction earthquakes and stress
696 interaction between the southern San Andreas and nearby thrust and strike-slip faults,
697 *Journal of Geophysical Research: Solid Earth*, *109*(B2),
698 doi:https://doi.org/10.1029/2003JB002607.
699 Liu, X., W. Xu, Z. He, L. Fang, and Z. Chen (2022). Aseismic slip and cascade triggering process
700 of foreshocks leading to the 2021 Mw 6.1 Yangbi Earthquake, *Seismological Research*
701 *Letters (in press)*.
702 Liu, Y., H. Yao, H. Zhang, and H. Fang (2021). The Community Velocity Model V.1.0 of
703 Southwest China, Constructed from Joint Body- and Surface-Wave Travel-Time
704 Tomography, *Seismological Research Letters*, doi:10.1785/0220200318.
705 López-Comino, J. A., and S. Cesca (2018). Source Complexity of an Injection Induced Event: The
706 2016 Mw 5.1 Fairview, Oklahoma Earthquake, *Geophysical Research Letters*, *45*(9),
707 4025-4032, doi:https://doi.org/10.1029/2018GL077631.
708 Madariaga, R. (1976). Dynamics of an expanding circular fault, *Bulletin of the Seismological*
709 *Society of America*, *66*(3), 639-666.
710 McLaskey, G. C. (2019). Earthquake Initiation From Laboratory Observations and Implications
711 for Foreshocks, *Journal of Geophysical Research: Solid Earth*, *124*(12), 12882-12904,
712 doi:https://doi.org/10.1029/2019JB018363.
713 Mendoza, M. M., A. Ghosh, M. S. Karplus, S. L. Klemperer, S. N. Sapkota, L. B. Adhikari, and
714 A. Velasco (2019). Duplex in the Main Himalayan Thrust illuminated by aftershocks of
715 the 2015 Mw 7.8 Gorkha earthquake, *Nature Geoscience*, *12*(12), 1018-1022,
716 doi:10.1038/s41561-019-0474-8.
717 Meng, H., and W. Fan (2021). Immediate Foreshocks Indicating Cascading Rupture Developments
718 for 527 M 0.9 to 5.4 Ridgecrest Earthquakes, *Geophysical Research Letters*, *48*(19),
719 e2021GL095704, doi:https://doi.org/10.1029/2021GL095704.
720 Meng, Q., S. Ni, and Z. Peng (2021). Complex Source Behaviors and Spatiotemporal Evolution
721 of Seismicity During the 2015–2016 Earthquake Sequence in Cushing, Oklahoma, *Journal*
722 *of Geophysical Research: Solid Earth*, *126*(6), e2021JB022168,
723 doi:https://doi.org/10.1029/2021JB022168.
724 Meng, X., and Z. Peng (2015). Increasing lengths of aftershock zones with depths of moderate-
725 size earthquakes on the San Jacinto Fault suggests triggering of deep creep in the middle
726 crust, *Geophysical Journal International*, *204*(1), 250-261, doi:10.1093/gji/ggv445.
727 Mignan, A. (2014). The debate on the prognostic value of earthquake foreshocks: A meta-analysis,
728 *Scientific Reports*, *4*(1), 4099, doi:10.1038/srep04099.
729 Parsons, T., and A. A. Velasco (2009). On near-source earthquake triggering, *Journal of*
730 *Geophysical Research: Solid Earth*, *114*(B10), doi:https://doi.org/10.1029/2008JB006277.
731
732 Peng, Z., and P. Zhao (2009). Migration of early aftershocks following the 2004 Parkfield
733 earthquake, *Nature Geoscience*, *2*(12), 877-881, doi:10.1038/ngeo697.
734 Perfettini, H., and J.-P. Avouac (2004). Postseismic relaxation driven by brittle creep: A possible
735 mechanism to reconcile geodetic measurements and the decay rate of aftershocks,
736 application to the Chi-Chi earthquake, Taiwan, *Journal of Geophysical Research: Solid*
737 *Earth*, *109*(B2), doi:https://doi.org/10.1029/2003JB002488.

738 Prieto, G. A., R. L. Parker, and F. L. Vernon Iii (2009). A Fortran 90 library for multitaper
739 spectrum analysis, *Computers & Geosciences*, *35*(8), 1701-1710,
740 doi:https://doi.org/10.1016/j.cageo.2008.06.007.
741 Roeloffs, E. A. (2006). Evidence for Aseismic Deformation Rate Changes Prior to Earthquakes,
742 *Annual Review of Earth and Planetary Sciences*, *34*(1), 591-627,
743 doi:10.1146/annurev.earth.34.031405.124947.
744 Ross, Z. E., and Y. Ben-Zion (2016). Toward reliable automated estimates of earthquake source
745 properties from body wave spectra, *Journal of Geophysical Research: Solid Earth*, *121*(6),
746 4390-4407, doi:https://doi.org/10.1002/2016JB013003.
747 Ruiz, S., M. Metois, A. Fuenzalida, J. Ruiz, F. Leyton, R. Grandin, C. Vigny, R. Madariaga, and
748 J. Campos (2014). Intense foreshocks and a slow slip event preceded the 2014 Iquique
749 M_w 8.1 earthquake, *Science*, *345*(6201), 1165-1169,
750 doi:10.1126/science.1256074.
751 Ruiz, S., et al. (2017). Nucleation Phase and Dynamic Inversion of the Mw 6.9 Valparaíso 2017
752 Earthquake in Central Chile, *Geophysical Research Letters*, *44*(20), 10,290-210,297,
753 doi:https://doi.org/10.1002/2017GL075675.
754 Shelly, D. R. (2020). A High-Resolution Seismic Catalog for the Initial 2019 Ridgecrest
755 Earthquake Sequence: Foreshocks, Aftershocks, and Faulting Complexity, *Seismological*
756 *Research Letters*, doi:10.1785/0220190309.
757 Shen, Z.-K., J. Lü, M. Wang, and R. Bürgmann (2005). Contemporary crustal deformation around
758 the southeast borderland of the Tibetan Plateau, *Journal of Geophysical Research: Solid*
759 *Earth*, *110*(B11), doi:10.1029/2004jb003421.
760 Steacy, S., J. Gomberg, and M. Cocco (2005). Introduction to special section: Stress transfer,
761 earthquake triggering, and time-dependent seismic hazard, *Journal of Geophysical*
762 *Research: Solid Earth*, *110*(B5), doi:https://doi.org/10.1029/2005JB003692.
763 Sun, Q., Z. Guo, S. Pei, Y. V. Fu, and Y. J. Chen (2022). Fluids Triggered the 2021 Mw 6.1 Yangbi
764 Earthquake at an Unmapped Fault: Implications for the Tectonics at the Northern End of
765 the Red River Fault, *Seismological Research Letters*, *93*(2A), 666-679,
766 doi:10.1785/0220210227.
767 Tape, C., S. Holtkamp, V. Silwal, J. Hawthorne, Y. Kaneko, J. P. Ampuero, C. Ji, N. Ruppert, K.
768 Smith, and M. E. West (2018). Earthquake nucleation and fault slip complexity in the lower
769 crust of central Alaska, *Nature Geoscience*, *11*(7), 536-541, doi:10.1038/s41561-018-
770 0144-2.
771 Toda, S., R. S. Stein, K. Richards-Dinger, and S. B. Bozkurt (2005). Forecasting the evolution of
772 seismicity in southern California: Animations built on earthquake stress transfer, *Journal*
773 *of Geophysical Research: Solid Earth*, *110*(B5),
774 doi:https://doi.org/10.1029/2004JB003415.
775 Uchida, N., T. Matsuzawa, W. L. Ellsworth, K. Imanishi, T. Okada, and A. Hasegawa (2007).
776 Source parameters of a M4.8 and its accompanying repeating earthquakes off Kamaishi,
777 NE Japan: Implications for the hierarchical structure of asperities and earthquake cycle,
778 *Geophysical Research Letters*, *34*(20), doi:https://doi.org/10.1029/2007GL031263.
779 Waldhauser, F. (2001). hypoDD--A program to compute double-difference hypocenter locations,
780 *U.S. Geological Survey Open-File Report 01-113*, 25 pp.
781 Wang, G., Z. Wu, G. Peng, Z. Liu, R. Luo, X. Huang, and H. Chen (2021). Seismogenic fault and
782 it's rupture characteristics of 21 May, 2021 Yangbi Ms6.4 earthquake: analysis results from
783 relocation of earthquake sequence, *Journal of Geomechanics (in Chinese)*, *27(4)*, 1-22.

Wang, K., Q.-F. Chen, S. Sun, and A. Wang (2006). Predicting the 1975 Haicheng Earthquake, *Bulletin of the Seismological Society of America*, *96*(3), 757-795, doi:10.1785/0120050191.

Wang, W., J. He, X. Wang, Y. Zhou, J. Hao, L. Zhao, and Z. Yao (2022). Rupture process models of the Yangbi and Maduo earthquakes that struck the eastern Tibetan Plateau in May 2021, *Science Bulletin*, *67*(5), 466-469, doi:https://doi.org/10.1016/j.scib.2021.11.009.

Wu, Q., X. Chen, and R. E. Abercrombie (2019). Source Complexity of the 2015 Mw 4.0 Guthrie, Oklahoma Earthquake, *Geophysical Research Letters*, *46*(9), 4674-4684, doi:https://doi.org/10.1029/2019GL082690.

Xu, S., B. Wang, L. M. Jones, X. Ma, and P. Shen (1982). The foreshock sequence of haicheng earthquake and earthquake swarm—the use of foreshock sequences in earthquake prediction, *Tectonophysics*, *85*(1), 91-105, doi:https://doi.org/10.1016/0040-1951(82)90079-8.

Yang, Z., J. Liu, X.-M. Zhang, W. Deng, G. Du, and X. Wu (2021). A preliminary report of the Yangbi, Yunnan, Ms6.4 earthquake of May 21, 2021, *Earth and Planetary Physics*, *5*(4), 1-3, doi:10.26464/epp2021036.

Yao, D., Y. Huang, Z. Peng, and R. R. Castro (2020). Detailed Investigation of the Foreshock Sequence of the 2010 Mw7.2 El Mayor-Cucapah Earthquake, *Journal of Geophysical Research: Solid Earth*, *125*(6), e2019JB019076, doi:https://doi.org/10.1029/2019JB019076.

Yoon, C. E., N. Yoshimitsu, W. L. Ellsworth, and G. C. Beroza (2019). Foreshocks and Mainshock Nucleation of the 1999 Mw 7.1 Hector Mine, California, Earthquake, *Journal of Geophysical Research: Solid Earth*, *124*(2), 1569-1582, doi:https://doi.org/10.1029/2018JB016383.

Yue, H., Z. E. Ross, C. Liang, S. Michel, H. Fattahi, E. Fielding, A. Moore, Z. Liu, and B. Jia (2017). The 2016 Kumamoto Mw = 7.0 Earthquake: A Significant Event in a Fault–Volcano System, *Journal of Geophysical Research: Solid Earth*, *122*(11), 9166-9183, doi:https://doi.org/10.1002/2017JB014525.

Yue, H., and T. Lay (2020). Resolving Complicated Faulting Process Using Multi-Point-Source Representation: Iterative Inversion Algorithm Improvement and Application to Recent Complex Earthquakes, *Journal of Geophysical Research: Solid Earth*, *125*(2), e2019JB018601, doi:https://doi.org/10.1029/2019JB018601.

Yue, H., J. Sun, M. Wang, Z. Shen, M. Li, L. Xue, W. Lu, Y. Zhou, C. Ren, and T. Lay (2021). The 2019 Ridgecrest, California earthquake sequence: Evolution of seismic and aseismic slip on an orthogonal fault system, *Earth and Planetary Science Letters*, *570*, 117066, doi:https://doi.org/10.1016/j.epsl.2021.117066.

Yun, N., S. Zhou, H. Yang, H. Yue, and L. Zhao (2019). Automated Detection of Dynamic Earthquake Triggering by the High-Frequency Power Integral Ratio, *Geophysical Research Letters*, *46*(22), 12977-12985, doi:https://doi.org/10.1029/2019GL083913.

Zhang, P., Q. Deng, G. Zhang, J. Ma, W. Gan, W. Min, F. Mao, and Q. Wang (2003). Active tectonic blocks and strong earthquakes in the continent of China, *Science in China Series D: Earth Sciences*, *46*(2), 13-24, doi:10.1360/03dz0002.

Zhang, Y., Y. An, F. Long, G. Zhu, M. Qin, Y. Zhong, Q. Xu, and H. Yang (2021). Short-Term Foreshock and Aftershock Patterns of the 2021 Ms 6.4 Yangbi Earthquake Sequence, *Seismological Research Letters*, *93*(1), 21-32, doi:10.1785/0220210154.

Zhou, Y., H. Yue, Q. Kong, and S. Zhou (2019). Hybrid Event Detection and Phase-Picking Algorithm Using Convolutional and Recurrent Neural Networks, *Seismological Research Letters*, *90*(3), 1079-1087, doi:10.1785/0220180319.

Zhou, Y., A. Ghosh, L. Fang, H. Yue, S. Zhou, and Y. Su (2021a). A High-Resolution Seismic Catalog for the 2021 Ms6.4/Mw6.1 YangBi Earthquake Sequence, Yunnan, China: Application of AI picker and Matched Filter, *Earthquake Science*, *34*(5), 390-398, doi:10.29382/eqs-2021-0031.

Zhou, Y., H. Yue, L. Fang, S. Zhou, L. Zhao, and A. Ghosh (2021b). An Earthquake Detection and Location Architecture for Continuous Seismograms: Phase Picking, Association, Location, and Matched Filter (PALM), *Seismological Research Letters*, *93*(1), 413-425, doi:10.1785/0220210111.

Zhu, L., and L. A. Rivera (2002). A note on the dynamic and static displacements from a point source in multilayered media, *Geophysical Journal International*, *148*(3), 619-627, doi:10.1046/j.1365-246X.2002.01610.x.

Ziv, A., and A. M. Rubin (2000). Static stress transfer and earthquake triggering: No lower threshold in sight?, *Journal of Geophysical Research: Solid Earth*, *105*(B6), 13631-13642, doi:https://doi.org/10.1029/2000JB900081.